sciendo

ARTIFICIAL SATELLITES, Vol. 57, No. 1 – 2022
DOI: 10.2478/arsa-2022-0004

RELIABILITY OF CSRS-PPP FOR VALIDATING THE EGYPTIAN GEODETIC CORS NETWORKS

Ashraf Abdallah[1], Tarek Agag[2]

[1] Faculty of Engineering, Aswan University, Aswan, Egypt
[2] Egyptian Surveying Authority, Giza, Egypt

email: ashraf.abdallah@aswu.edu.eg, tarekagag_2001@yahoo.com

ABSTRACT. The development, utilization, and maintenance of continuously operating reference stations (CORS) network are vital in many areas of surveying and geodesy, such as controlling geodetic networks, developing local ionospheric models, and estimating the tectonic plate movements. Accordingly, the Egyptian Surveying Authority (ESA) established a CORS network consisting of 40 stations covering the Nile valley and its delta in 2011. CORS collect global navigation satellite system (GNSS) data. Recently, Egypt has witnessed rapid growth in many infrastructure projects and the development of new cities on a national scale. Therefore, there is an urgent need to investigate the ESA-CORS accuracy; the quality of data from the ESA-CORS must be considered for monitoring continuous tectonic motion, coordinating changes, and for Egypt's development plan. Contemporary research worldwide identified considerable benefits of the precise point positioning (PPP) solution of dual- or single-frequency GNSS data. This study investigates the reliability of using the CSRS-PPP service for three consecutive observation days of 32 ESA-CORS networks in Egypt and the surrounding six international GNSS services (IGS)-CORS. For ESA-CORS, the PPP solution showed a root mean square error (RMSE) value of 6 mm (standard deviation [SD] = 3–4 mm) in east and north; for the height direction, the solution indicated an RMSE value of 22 mm (SD was about 14 mm). At a confidence level of 95%, this study revealed that $SD_{95\%}$ was 2 mm in east and north directions and 6–7 mm for the height direction. This study shows that the PPP solution shown from the ESA-CORS stations is associated with two times better for horizontal and four times for the height direction than the delivered form ESA-CORS stations.

Keywords: GNSS-PPP, CSRS-PPP, Egypt, CORS network

1. INTRODUCTION

The global navigation satellite system (GNSS) techniques are effective for monitoring landslides and earth movement in high-rise and coastal regions. The GNSS techniques support construction activities against earthquake effects, leading to an early warning for the catastrophic crisis and risk management. The US National Oceanic and Atmospheric Administration's (NOAA's) national geodetic survey (NGS) introduced the concept of continuously operating reference stations (CORS) two decades ago. This system is designed to provide users with the geodetic latitude, longitude, height, orthometric height, geopotential, acceleration of gravity, and vertical deflection at any point in the USA (Snay & Soler 2008).

The international GNSS service (IGS) provides a worldwide collection of CORS network stations. Walpersdorf et al. (2007) reported that the IGS stations in Africa have many characteristics. The network is mainly situated in a coastal area with long baselines, and this location affects the accuracy of network precision. In addition, the network is very active with ionosphere activities.

Egypt is rapidly undertaking many infrastructure projects such as highways, railway projects, and the construction of many new cities. One of the main obstacles in obtaining reliable continuous GNSS solutions is the lack of coverage for IGS stations. Consequently, the Egyptian Surveying Authority (ESA) established the first permanent Egyptian CORS network in January 2012. The network consisted of 40 stations covering mainly the Nile valley and its delta (Figure 1). Furthermore, according to the ESA (2012), the network was adjusted relative to the International Terrestrial Reference Frame (ITRF) system at the epoch October 23, 2011 (ITRF 2020). Moreover, the ESA older national passive GNSS reference network, called the high-accuracy reference network (HARN) (Figure 1), established in 1995, was referenced to the ITRF1994 (epoch 1996).

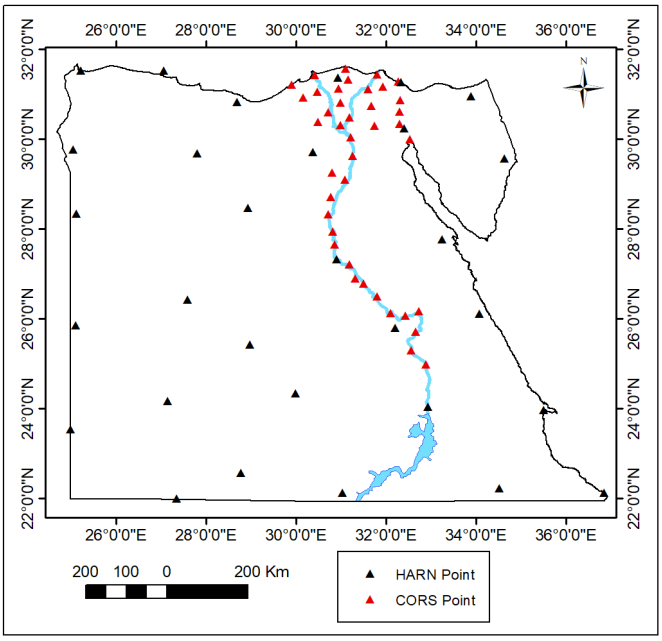

Figure 1. Layout of ESA-CORS and HARN stations

Zumberge et al. (1997) introduced the precise point positioning (PPP) estimation model two decades ago. The PPP technique that requires just one GNSS receiver faces many error sources, and these errors need to be modeled or eliminated. Four types of errors are considered: satellite-dependent, receiver-dependent, atmospheric (troposphere and ionosphere), and geophysical errors, including solid earth tides, polar tides, ocean tidal loading, and atmospheric tidal loading. Several software packages and online services provide the PPP solution (Table 1).

Researchers have recently shown increasing interest in evaluating the PPP accuracy of CORS network in Africa. Abdallah (2015) investigated different static PPP solutions for four CORS in Germany and found that solutions reached centimeter-level accuracy using the static technique for a convergence time of 24 h. This result matched the one obtained by Ayhan and Almuslmani (2021). In addition, Abdallah and Schwieger (2016) introduced a study of the PPP solution for the IGS-CORS in Africa. They concluded that the PPP solution obtained using (Canadian Spatial Reference System) CSRS-PPP online service produced three-dimensional (3D) root mean square error (RMSE) between 4 and 6 mm. Similar results based on GNSS

datasets in Egypt were reported by El Shouny and Miky (2019) and El Manaily et al. (2017). Rabah et al. (2016) proposed the utilization of PPP for geodetic datum maintenance and update in Egypt. Jamieson and Gillins (2018) determined the accuracy of static PPP solution for a static campaign, which consisted of six stations with 10 h of observation data. The study showed less than 1 and 1.5 cm accuracies for the horizontal and vertical directions, respectively. To evaluate the accuracy of the new Nigerian GNSS network (NIGNET), Isioye et al. (2019) studied different PPP online services with different observation durations (1, 2, and 6 h, and up to 24 h). The study used free online PPP services (e.g., GNSS Analysis and Positioning Software (GAPS-PPP) and magicGNSS). They found that the online GNSS PPP processing services can provide users with reliable results. Further, the results showed that the 24-h observation files produced results with a millimeter to centimeter level of accuracy by processing with magicGNSS and GAPS-PPP services.

This study aims to contribute to this growing area of research by exploring the accuracy of static PPP solutions for the Egyptian permeant CORS (ESA-CORS). The observation data of ESA-CORS are accessible only for the ESA and unavailable for users. Therefore, this paper assesses the significance and reliability of using CSRS-PPP as a solution to obtain a geodetic coordinate, such as a static PPP solution. The overall structure of the study comprises five sections, including this introductory section. Section 2 begins by laying out the theoretical approach of PPP solution and explaining the processing parameters using CSRS-PPP online service. Section 3 discusses the dataset and evaluation methodology. Section 4 presents the analysis and discusses the results obtained. Finally, the conclusion provides a summary of our findings.

Table 1. List of available PPP software and free online services

Software package		**Provider**
PPP software package	gLAB	Research group of Astronomy and Geomatics (gAGE) from the Universitat Politecnica de Catalunya (UPC) (Sanz et al. 2012)
	Net_Diff	GNSS Analysis Center, Shanghai Astronomical Observatory, Chinese Academy of Sciences (https://github.com/YizeZhang/Net_Diff)
	PRIDE PPP-AR	GNSS Research Center of Wuhan University, China (https://geodesy.noaa.gov/gps-toolbox/PRIDE.htm)
	GAMP	Research group at the German Research Centre for Geosciences GFZ (Zhou et al. 2018)
	Bernese GNSS V. 5.2	Astronomical Institute of the University of Bern (AIUB), Switzerland (Dach & Walser 2015)
	GIPSY-OASIS II	Jet Propulsion Laboratory (JPL), California Institute of Technology, USA (https://gipsy-oasis.jpl.nasa.gov/index.php?page=software)
	RTKLIB	Tomoja Takasu at Tokyo University Marine Science and Technology, Japan (http://www.rtklib.com/)
	NAPEOS	European Space Agency (http://www.esa.int/Enabling_Support/Operations/NAPEOS)
	GAMIT/GLOBK	Department of Earth, Atmospheric, and Planetary Sciences at the Massachusetts Institute of Technology (MIT) (http://geoweb.mit.edu/gg/)

Software package		Provider
PPP free online service	CSRS-PPP	Canadian Geodetic Survey (CGS) (https://webapp.geod.nrcan.gc.ca/geod/tools-outils/ppp.php)
	APPS-PPP	Jet Propulsion Laboratory (JPL), California Institute of Technology, USA (http://apps.gdgps.net/)
	GAPS-PPP	GNSS Analysis and Positioning Software, Department of Geodesy and Geomatics Engineering University of New Brunswick (http://gaps.gge.unb.ca/)
	magicGNSS	GMV Aerospace and Defence S.A., Spain (https://magicgnss.gmv.com/)

2. PRECISE POINT POSITIONING

As shown in equations (1)–(4), the PPP position is determined based on the processing of the following ionosphere-free combination of the undifferenced code ($\rho^S_{R\ IF}$), and phase ($\Phi^S_{R\ IF}$) of multi-constellation GNSS observations (Hofmann-Wellenhof, Lichtenegger & Wasle 2008; and Misra & Enge 2012). The first order of the ionospheric delay is eliminated for dual-frequency receivers using the ionospheric-free linear combination (IF). This combination does not eliminate the full ionosphere refractions. The higher order that ranges from sub-millimeters to several centimeters is considered for highly accurate applications such as surveying CORS coordinates (Kedar et al. 2003).

$$\rho = r + c(\delta^R - \delta^S) + \Delta_{\text{iono}} + \Delta_{\text{trop}} + \Delta_{\text{sol}} + \Delta_{\text{pol}} + \Delta_{\text{ocn}} + \Delta_{\text{atm}} + \Delta_{\text{mul}} + \in_\rho \quad (1)$$

$$\lambda\Phi = r + c(\delta^R - \delta^S) - + \Delta_{\text{trop}} + \lambda\text{N} + \Delta_{\text{sol}} + \Delta_{\text{pol}} + \Delta_{\text{ocn}} + \Delta_{\text{atm}} + \Delta_{\text{mul}} + \Delta_{\text{pcv}} + \lambda\text{w} + \in_\Phi \quad (2)$$

$$\rho^S_{R\ \text{IF}} = \frac{f_{l1}^2\,\rho_{l1} - f_{l2}^2\,\rho_{l2}}{(f_{l1}^2 - f_{l2}^2)} = 2.546\rho_{l1} - 1.546\rho_{l2} \quad (3)$$

$$\Phi^S_{R\ \text{IF}} = \frac{f_{l1}^2\,\Phi_{l1} - f_{l2}^2\,\Phi_{l2}}{(f_{l1}^2 - f_{l2}^2)} = 2.546\Phi_{l1} - 1.546\Phi_{l2} \quad (4)$$

where:

Δ_{iono} is the ionospheric delay,
Δ_{trop} is the tropospheric delay,
Δ_{sol} is the solid earth tides error,
Δ_{pol} is the pole tides error,
Δ_{ocn} is the ocean loading effect,
Δ_{atm} is the atmospheric loading effect,
Δ_{mul} is the multipath effect,
Δ_{pcv} is the antenna phase center variation,
w is the correction of phase wind-up,
δ^R is the receiver clock bias,
δ^S is the satellite clock bias,
c is the speed of light,
r is the true range between receiver (x_R, y_R, z_R) and satellite (x_S, y_S, z_S) coordinates,
λ is the carrier wavelength,
N is the ambiguity integer,
$\rho^S_{R\ \text{IF}}$ is the ionosphere-free combination of code ranges,

$\Phi_{R\,\mathrm{IF}}^{S}$ is the ionosphere-free combination of carrier phases,
f_{L1}, f_{L2} are the GNSS frequencies of L1 and L2 signals, respectively,
ρ_{l1}, ρ_{l2} are the code ranges of L1 and L2 signals, respectively,
Φ_{L1}, Φ_{L2} are the carrier phases of L1 and L2 signals, respectively,
and $\in_{\rho}$ and $\in_{\Phi}$ are the relevant measurement noises.

The tropsphereic zenith delay (Δ_{trop}) consi sts of dry and wet components. The dry component (zenith hydrostatic delay) is about 90% of the delay; this part can be modeled using mathematical models. The wet component (zenith wet delay) is unpredictable; it depends on water vapor and is typically less than 30 cm (Hofmann-Wellenhof, Lichtenegger & Wasle 2008; Bar-Sever, Kroger & Borjesson 1998). The total tropospheric zenith delay is expressed in equation (5). Due to the consideration of the arbitrary zenith angle of the signal, the estimation of the delay is expressed in the function of the elevation angle of the satellite E. Equation (6) estimates the tropospheric delay relating to the mapping function for the dry m_h and wet parts m_w (Misra & Enge 2012).

$$\Delta_{\mathrm{trop}} = T_z^h + T_z^w \tag{5}$$

$$\Delta_{\mathrm{trop}}(E) = T_z^h \cdot m_h(E) + T_z^w \cdot m_w(E) \tag{6}$$

Table 2 presents the processing parameters of CSRS-PPP software. The reference system for the software is based on ITRF 2014 (epoch 2019 according to measurement date); the obtained coordinates have Cartesians XYZ format and Ellipsoidal/(Universal Transverse Mercator) UTM system. The IGS final ephemerides are used during processing with a satellite orbit of a 15-min interval and a satellite clock of a 30-s interval. The ionospheric delay is eliminated for dual-frequency data using the ionospheric-free linear combination, and the second-order errors are equally considered. For single-frequency data, the ionospheric delay is modeled using the final global ionospheric maps (GIM) from IGS. Regarding the tropospheric delay, the processing tool that is based on the global pressure and temperature (GPT) model uses the Davis model for the hydrostatic delay. For the wet part, the processing mechanism uses the Hopfield model that is based on the GPT model. In addition, the Vienna mapping function (VMF1) is utilized (Boehm, Werl & Schuh 2006). The satellite and receiver antenna phase variations are based on the IGS-ANTEX (NGS 2021) format (CSRS-PPP 2021). Furthermore, the PPP-based coordinates in ITRF 2014 (epoch 2019) were compared with the recent network adjustment in the same frame and epoch.

Table 2. CSRS-PPP processing parameters

Item	**Processing parameter**
GNSS system	GPS and GLONASS
Reference system	ITRF2014 (epoch 2019)
Coordinate format	XYZ/Ellipsoidal/UTM
Satellite orbit and clock ephemeris	IGS final (Orbit: 15-minute interval & clock: 30-second interval)
Satellite phase center offsets	IGS-ANTEX (NGS 2021)
Receiver phase center offsets	IGS-ANTEX (NGS 2021)
Elevation angle	7.5°
Sampling rate	30 s

Item	Processing parameter
Ionospheric model	Linear ionosphere-free combination + second-order parameters
Tropospheric model	Dry: Davis (GPT) (Sakurai 1985; Kouba 2009) Wet: Hopfield model (GPT) (Hopfield 1969; Kouba 2009) VMF1 (Böhm & Schuh 2004)
Software	CSRS-PPP
Observation data	Single/dual frequency and static/kinematic
Data transfer	Email
Ocean tide loading	FES 2004 (Le Provost & Lyard 1997)

3. DATASET AND EVALUATION METHODOLOGY

Overall, 32 ESA-CORS were analyzed for three consecutive days (DOY: 201–203/2019) with an observation interval of 30 s (Figure 2a) using CSRS-PPP online service (see Table 2). For global impact, six IGS-CORS were also processed for the same observation days (Figure 2b); these stations are surrounding Egypt. The complete list of processed stations is presented in Table 3. The height of ESA-CORS varied between 30 and 149 m. Moreover, the height of IGS-CORS (shadowed stations in Table 3) varied between 31 and 886 m. Figure 2a shows the ESA-CORS and Figure 2b shows the IGS-CORS.

(a) (b)

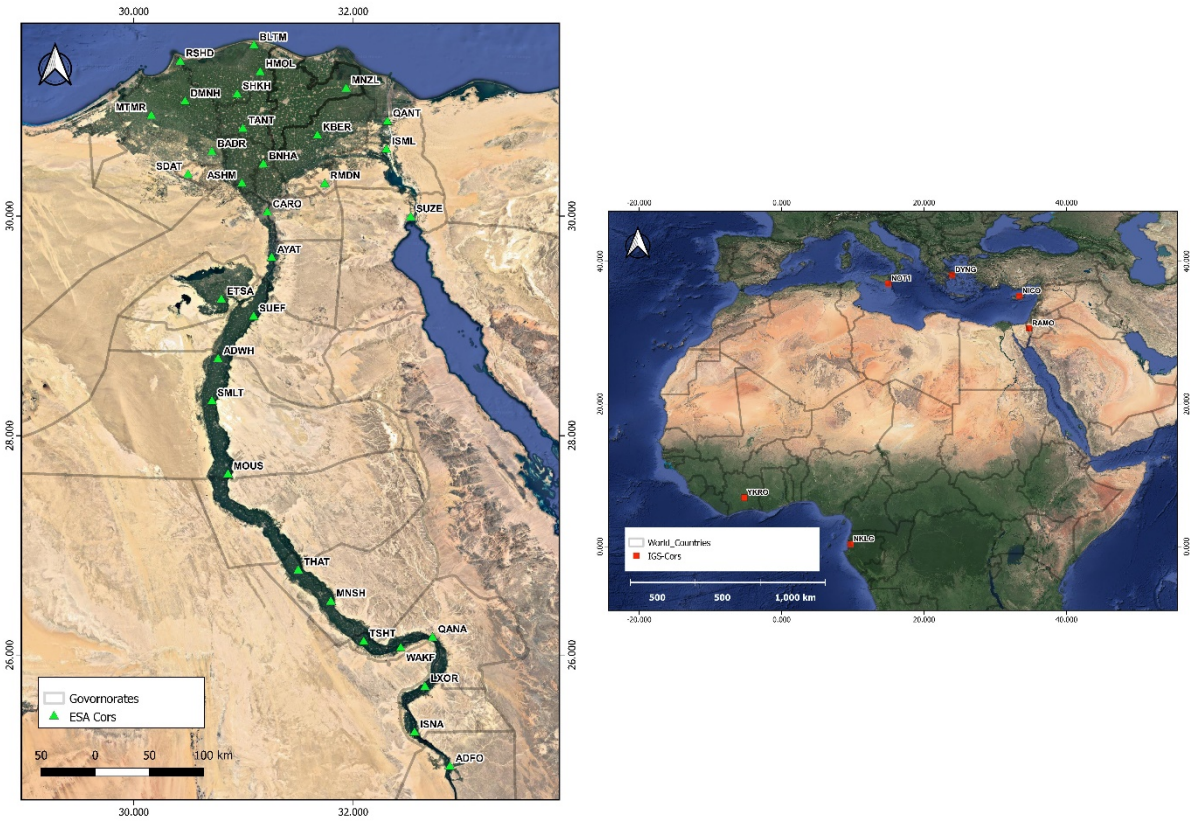

Figure 2. Design of global constrained network solution ©Google Earth:
(a) ESA-CORS, (b) IGS-CORS

Table 3. List of CORS

Station ID	Latitude	Longitude	H	Station ID	Latitude	Longitude	H
ADFO	N24°58'46.241"	E32°52'49.913"	105.97	QANA	N26°09'22.293"	E32°43'18.173"	101.20
ADWH	N28°41'41.549"	E30°46'01.677"	64.61	QANT	N30°51'27.105"	E32°18'36.257"	34.11
ASHM	N30°17'40.001"	E30°59'04.720"	39.67	RMDN	N30°17'26.508"	E31°44'23.437"	149.50
AYAT	N29°37'06.841"	E31°15'22.315"	58.82	RSHD	N31°24'19.102"	E30°25'17.957"	36.85
BADR	N30°34'57.049"	E30°42'37.032"	47.94	SDAT	N30°22'31.934"	E30°29'34.676"	71.50
BLTM	N31°33'11.924"	E31°05'40.480"	30.37	SHKH	N31°06'24.609"	E30°56'26.923"	30.55
BNHA	N30°28'15.304"	E31°10'45.118"	46.02	SMLT	N28°18'38.917"	E30°42'39.376"	71.19
CARO	N30°01'55.725"	E31°12'55.058"	75.57	SUEF	N29°04'53.755"	E31°05'30.069"	60.47
DMNH	N31°02'27.912"	E30°27'57.358"	41.63	SUZE	N29°59'18.836"	E32°31'19.498"	47.13
ETSA	N29°14'15.413"	E30°47'49.999"	41.64	TANT	N30°47'36.413"	E30°59'35.224"	40.81
HMOL	N31°18'35.684"	E31°09'02.195"	44.08	THAT	N26°46'09.649"	E31°29'50.601"	87.69
ISML	N30°36'15.307"	E32°18'00.940"	43.27	TSHT	N26°07'06.090"	E32°05'40.335"	88.37
ISNA	N25°17'20.274"	E32°33'28.518"	102.49	WAKF	N26°03'41.760"	E32°25'52.706"	109.83
KBER	N30°43'56.659"	E31°40'21.508"	33.15	DYNG	N38°04'42.788"	E23°55'56.765"	510.56
LXOR	N25°42'29.159"	E32°39'09.500"	110.58	NICO	N35°08'27.558"	E33°23'47.216"	190.02
MNSH	N26°29'00.621"	E31°47'39.230"	96.24	NKLG	N00°21'14.072"	E09°40'19.660"	31.49
MNZL	N31°09'36.216"	E31°56'04.274"	36.95	NOT1	N36°52'33.049"	E14°59'23.246"	126.35
MOUS	N27°38'36.827"	E30°51'27.876"	82.44	RAMO	N30°35'51.388"	E34°45'47.314"	886.84
MTMR	N30°54'45.358"	E30°09'31.184"	33.16	YKRO	N06°52'14.023"	W05°14'24.327"	270.26

To obtain the reference solution of ESA-CORS, Trimble Business Center (TBC) V 5.0 was used to process our geodetic network. The final precise satellite orbits ".SP3" and the satellite clock corrections ".clk" were downloaded from the IGS website and included in data processing. To achieve such a high-precision GNSS solution, ionospheric and tropospheric delays as well as ocean tide loading were considered. The processing strategy consisted of two steps: firstly, six ESA-CORS (ADFO, ALEX, CARO, MOUS, QANT, and SUZE) were first processed with six tied IGS-CORS (YKRO, DYNG, NICO, NKLG, NOT1, and RAMO). The reference solution for IGS-stations was obtained from http://sopac-old.ucsd.edu/sector.shtml. These ESA-CORS were selected to cover the marginal borders of the permanent stations. In the second step, a local constrained network solution was solved depending on the previous six ESA-CORS that were solved from the global network. The overall local network consisted of 32 ESA-CORS. Figure 3 shows the network solution procedure.

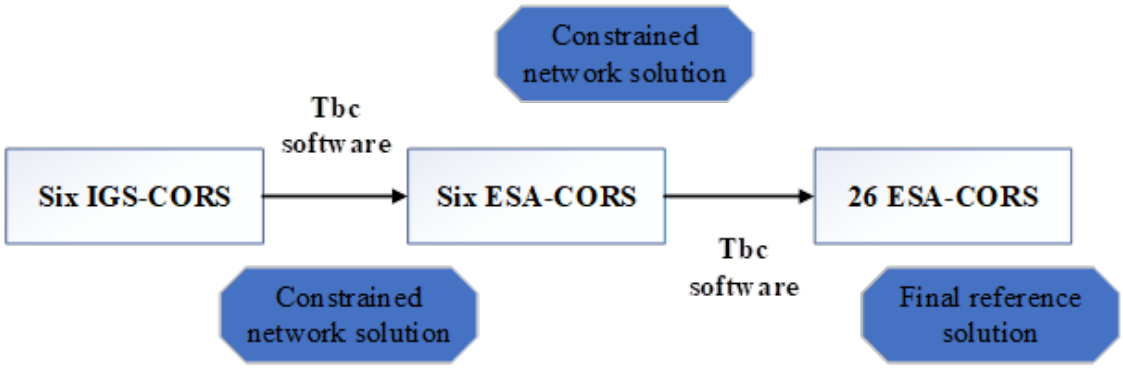

Figure 3. Network solution

As shown in equation (7), the evaluation methodology is presented using estimation of the error values $\delta_{i,j}$ between the reference coordinates m and the PPP solution m'. i refers to the number of epochs, and j refers to the east, north, and ellipsoidal height. For statistical evaluation in each direction, the RMSE, which refers to the error relative to the reference coordinates, is estimated using equation (8); n refers to the total number of epochs. In addition, the standard deviation (SD), which refers to the mean value for each direction μ, is calculated using equation (9) (Mikhail 1976). Finally, the confidence level of 95% is calculated for the SD values ($SD_{95\%}$) (see Figure 4).

$$\delta_{i,j} = m - m' \tag{7}$$

$$\text{RMSE} = \sqrt[2]{\frac{1}{n}\sum_{i=1}^{n}\left(\delta_{i,j}\right)^2} \tag{8}$$

$$\text{SD} = \sqrt[2]{\frac{1}{n-1}\sum_{i=1}^{n}\left(\delta_{i,j} - \mu\right)^2} \tag{9}$$

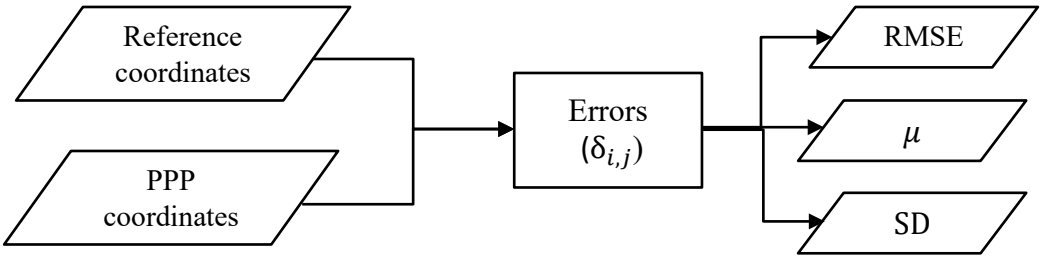

Figure 4. Processing schedule

4. ANALYSIS AND DISCUSSION

To assess the results, the consistency of results obtained from each case study should be evaluated separately.

a) **ESA-CORS:**

In Figure 5, the accuracy obtained in east, north, and height directions for DOY 201–202 and 203/2019 is presented. Furthermore, Table 4 shows the estimated statistics for all stations for the three consecutive days and the mean values. This table also shows the calculated values of maximum, mean, minimum error values, RMSE, and SD. $SD_{95\%}$ is estimated by excluding the outliers.

For DOY 201, the horizontal components showed an error of up to 20 mm with an average value of 4–6 mm using an RMSE of 6–7 mm (SD = 4 mm). Only ADWH, BADR, QANA, ADFO, and WAKF stations showed an error between 1 and 1.5 cm. It is clear from the result obtained that the error presented a value of up to 44 mm (μ = 18.5 mm) in the height direction with an RMSE of 22 mm (SD = 13 mm). From this data, we can determine the greatest height errors among the stations BADR, BLTM, ISNA, LXOR, MNSH, MOUS, QANA, RSHD, THAT, TSHT, and WAKF. No significant differences were found between DOY201 and DOY202 for horizontal direction; in the height direction, the component showed an error of up to 48 mm (μ = 17.4 mm). As shown in Table 4, the results indicated that the RMSE was 22.7 mm (SD = 14.8 mm). The themes from Figure 5 show that the extreme height errors were identified from the stations BLTM, ISAN, LXOR, MNSH, MOUS, QANA, THAT, TSHT, and WAKF.

The error for DOY203 was up to 10 mm (μ = 4 mm) for horizontal direction and up to 48 mm (μ = 17.6 mm) for height direction (Table 4). The estimated RMSE was 5 mm (SD = 2–4 mm) and 22 mm (13.7 mm) for horizontal and height directions, respectively. The stations that reported high errors in the height direction matched the ones reported for DOY202. The average errors of all days were up to 13 mm for horizontal (μ = 4–6 mm) and up to 47 mm (μ was circa 8 mm) for height direction. The obtained RMSE values were 6 mm (SD = 3–4 mm) for horizontal and 22 mm (SD was about 14 mm) for height direction. For a confidence level of 95%, the overall $SD_{95\%}$ was 2 mm for horizontal and 6–7 mm for height direction.

Table 4. Statistics of static-PPP solution for ESA-CORS in millimeters

	DOY201			**DOY202**			**DOY203**			**Overall mean values**		
	E	**N**	**h**	**E**	**N**	**h**	**E**	**N**	**h**	**E**	**N**	**h**
Max.	20.0	15.0	44.0	10.0	15.0	48.0	9.0	10.0	48.0	13.0	13.3	46.7
μ	6.5	4.2	18.5	6.0	4.6	17.4	4.3	4.2	17.6	5.6	4.3	17.8
Min.	0.0	1.0	0.0	1.0	0.0	0.0	0.0	0.0	0.0	0.3	0.3	0.0
RMSE	7.7	5.6	22.3	6.4	5.8	22.7	4.8	5.0	22.2	6.3	5.5	22.4
SD	4.2	3.8	12.8	2.3	3.6	14.8	2.1	3.8	13.7	2.9	3.7	13.8
$SD_{95\%}$	2.1	1.8	5.8	2.0	1.8	6.3	1.9	1.8	7.0	2.0	1.8	6.4

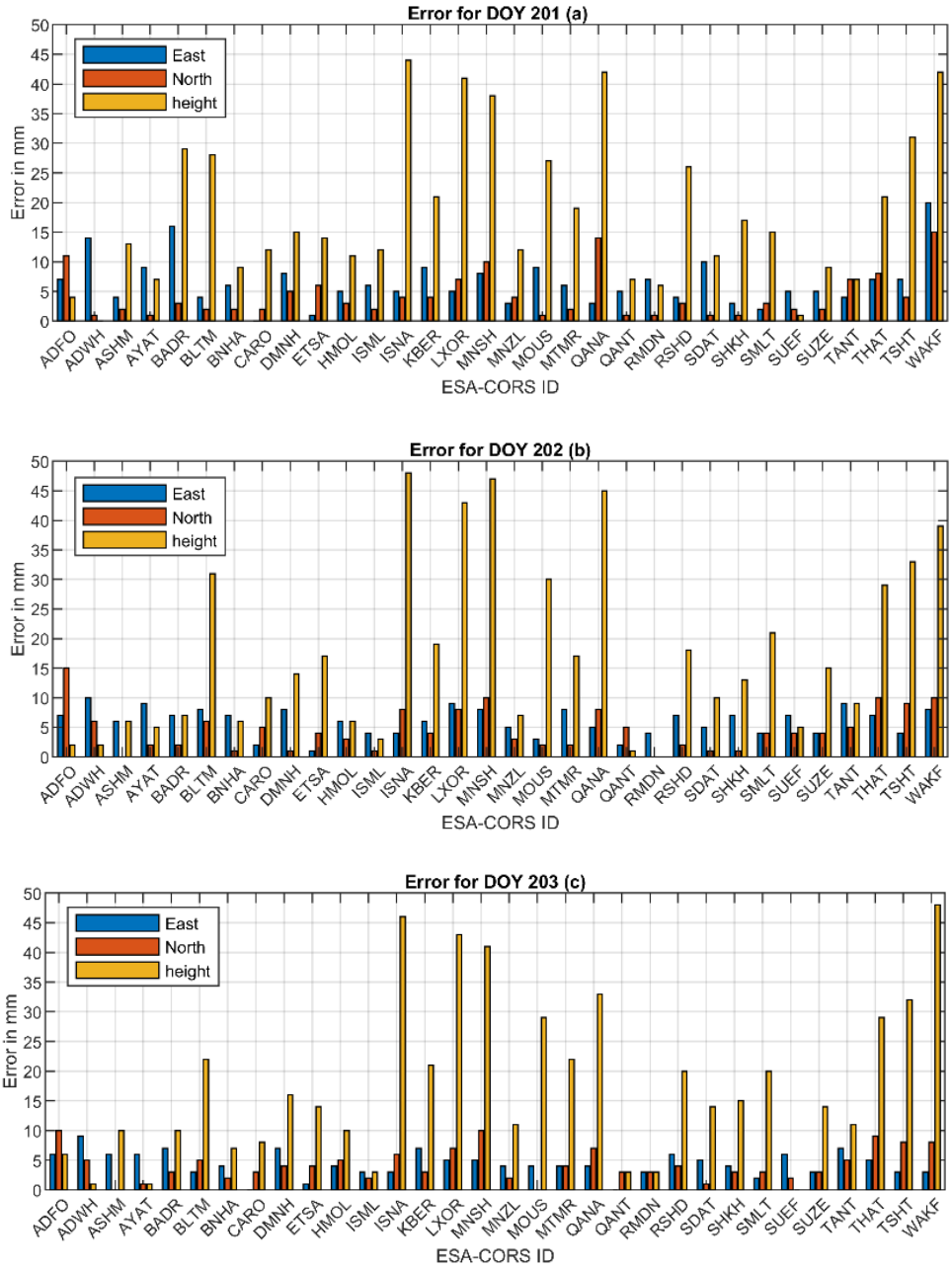

Figure 5. Dual PPP errors for ESA-CORS: (a) for DOY 201, (b) for DOY 202, and (c) for DOY 203 (static mode)

Three stations continuously lacked observation data for 1 day or three successive days (Table 5). In addition to the tabulated stations, other stations also had some losses in the observation data for various epochs. These continuous lacks or small losses affected the quality of PPP solutions. ADFO station lacked data for 4 h at the beginning of DOY 201, and the data also had some other losses (see Figure 6). However, some high errors were reported in the north direction. ADWH station lacked observation data for 1 h on DOY 201, which yielded a high error in the east direction. Furthermore, ASHM and AYAT stations had continuous observation data that reflected the high error in height direction for DOY 201. BADR station had an extreme lack of observation data for DOY 201, which led to high errors. For stations BLTM, DMNH, KBER, QANA, and TSHT, the continuous lack of observation data decreased PPP accuracy in the height direction. Several issues were identified for ISNA, LXOR, MNSH, MOUS, MTMR, RSHD, SMLT, and THAT stations; the solution reported a high error for height direction due

to several data losses during the convergence time for the 3 days. Finally, WAKF station had a high error for the height direction for DOY 202/203. The possible reason for the losses is bad Global System for Mobile Communications (GSM) transfer for the observation data to the center in Cairo, especially for the stations in Upper Egypt (e.g., WAKF, ISNA, LXOR, and MNSH).

Table 5. Statistics of continuous lack of observation data for ESA-CORS

Station ID	DOY 201	DOY 202	DOY 203	Station ID	DOY 201	DOY 202	DOY 203
ADFO	4 h	-	-	QANA	9 h	9 h	9 h
ADWH	1 h	-	-	QANT	1 h	-	-
BLTM	6 h	12 h	8 h	RMDN	3 h	-	-
DMNH	13 h	6 h	5 h	THAT	1 h	-	-
ISNA	2 h	-	-	TSHT	8 h	-	-
KBER	16 h	16 h	16 h	WAKF	22 h	-	-
MNSH	1 h	-	-				

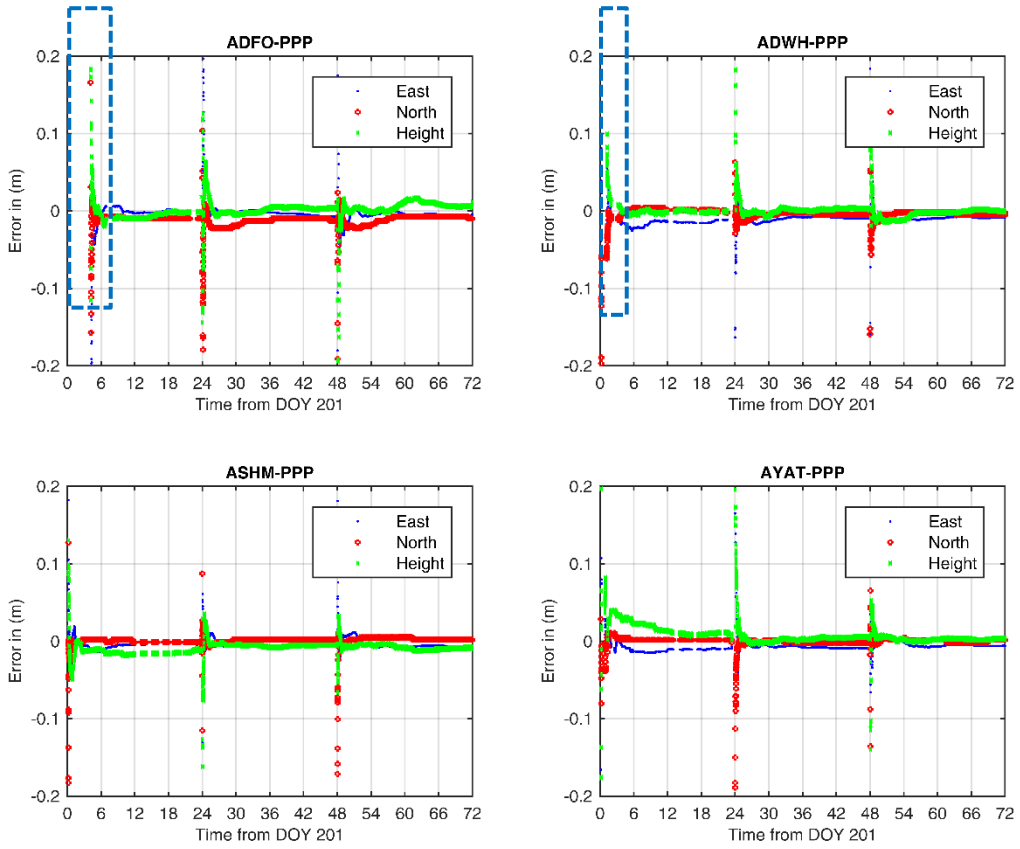

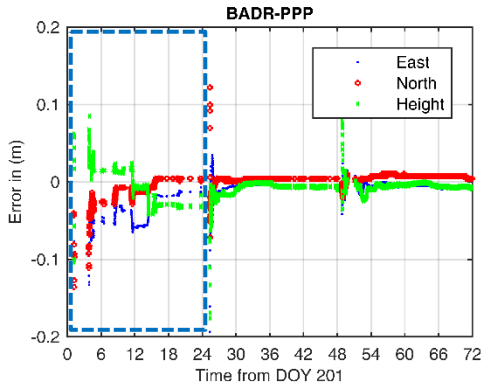
BADR-PPP
East
North
Height
Error in (m)
Time from DOY 201

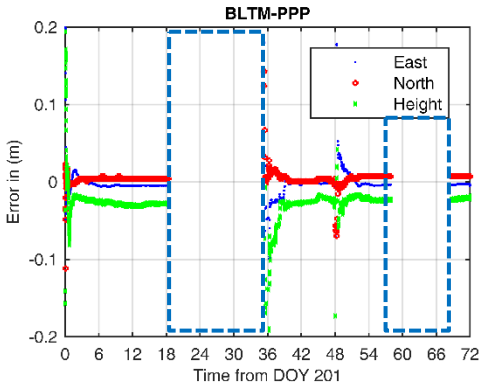
BLTM-PPP
East
North
Height
Error in (m)
Time from DOY 201

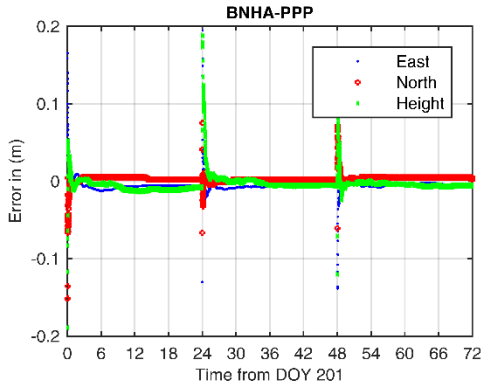
BNHA-PPP
East
North
Height
Error in (m)
Time from DOY 201

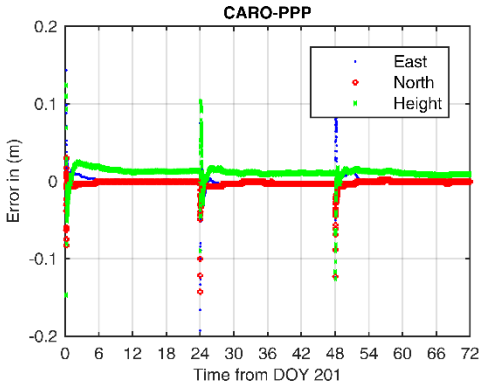
CARO-PPP
East
North
Height
Error in (m)
Time from DOY 201

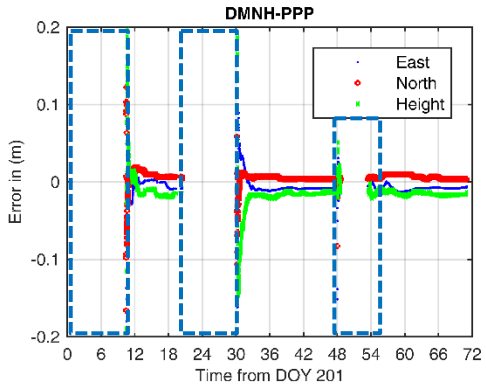
DMNH-PPP
East
North
Height
Error in (m)
Time from DOY 201

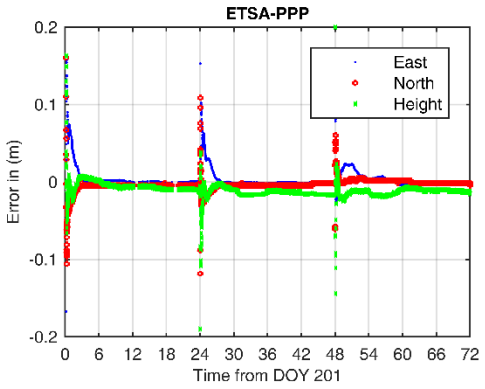
ETSA-PPP
East
North
Height
Error in (m)
Time from DOY 201

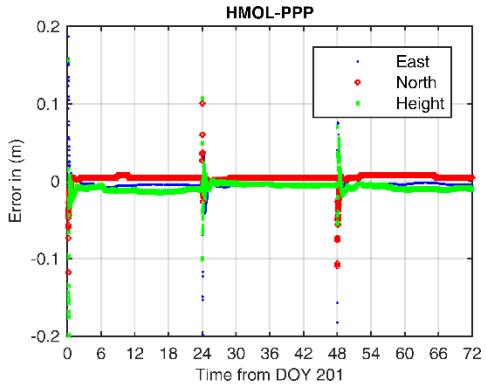
HMOL-PPP
East
North
Height
Error in (m)
Time from DOY 201

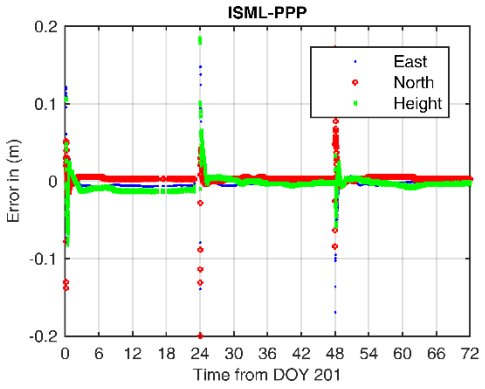
ISML-PPP
East
North
Height
Error in (m)
Time from DOY 201

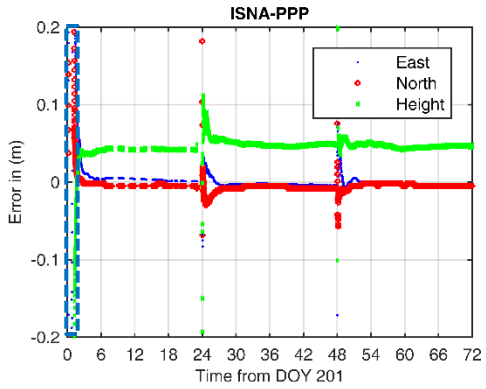
ISNA-PPP
East
North
Height
Error in (m)
Time from DOY 201

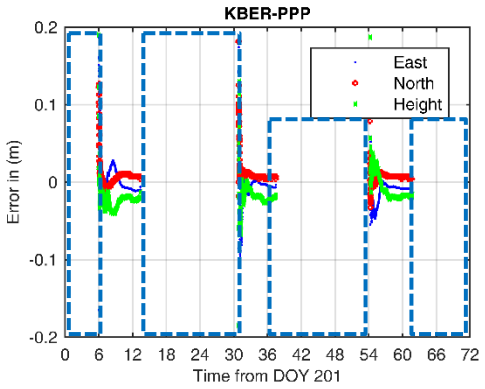
KBER-PPP
East
North
Height
Error in (m)
Time from DOY 201

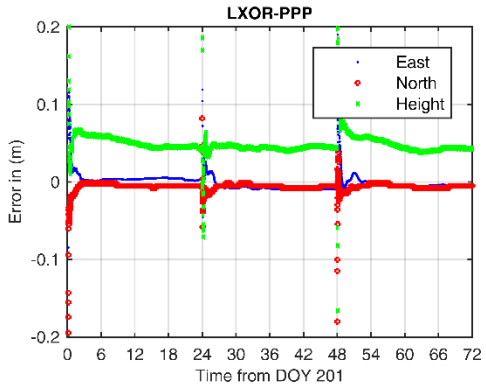
LXOR-PPP
East
North
Height
Error in (m)
Time from DOY 201

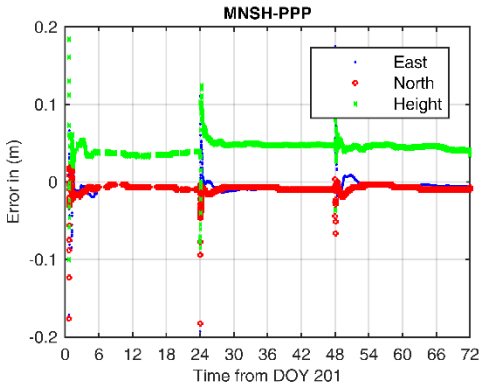
MNSH-PPP
East
North
Height
Error in (m)
Time from DOY 201

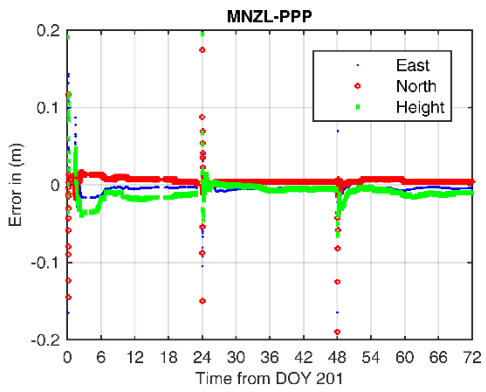
MNZL-PPP
East
North
Height
Error in (m)
Time from DOY 201

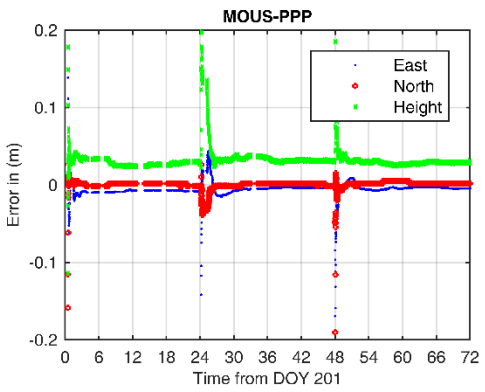
MOUS-PPP
East
North
Height
Error in (m)
Time from DOY 201

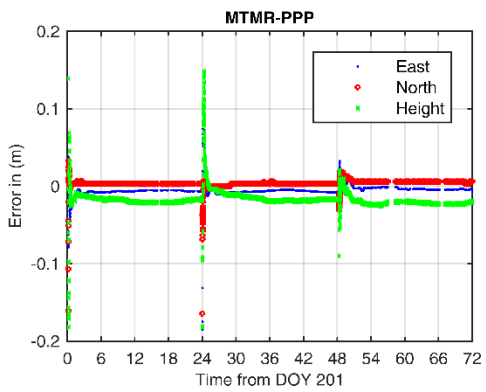
MTMR-PPP
East
North
Height
Error in (m)
Time from DOY 201

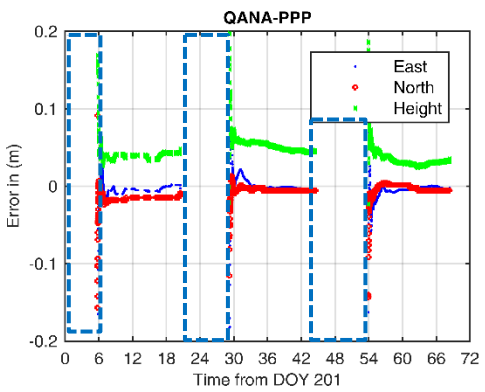
QANA-PPP
East
North
Height
Error in (m)
Time from DOY 201

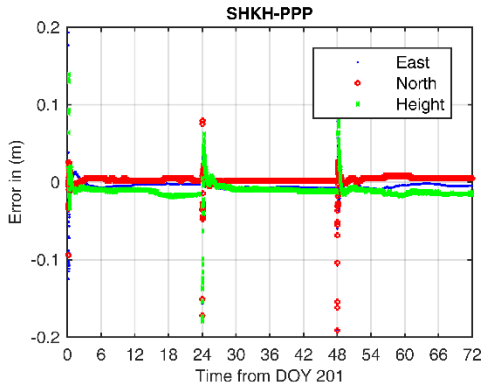
SHKH-PPP
East
North
Height
Error in (m)
Time from DOY 201

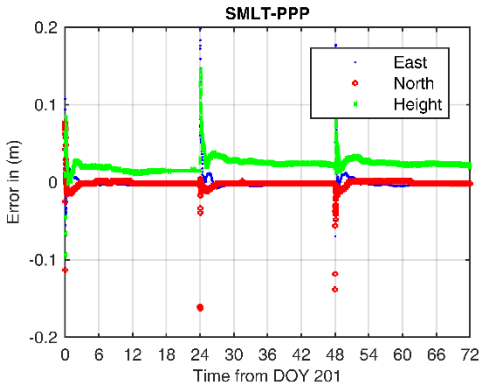
SMLT-PPP
East
North
Height
Error in (m)
Time from DOY 201

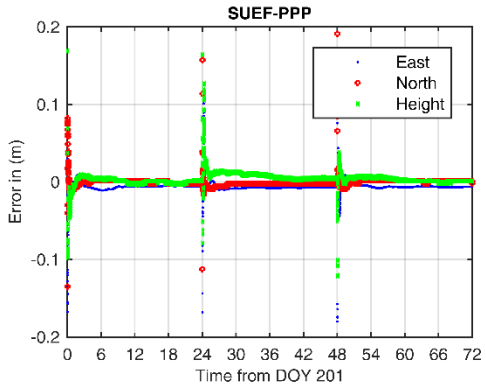
SUEF-PPP
East
North
Height
Error in (m)
Time from DOY 201

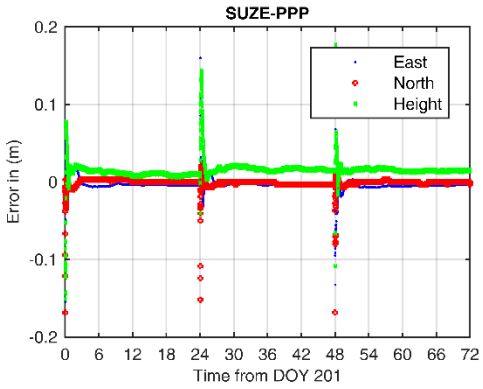
SUZE-PPP
East
North
Height
Error in (m)
Time from DOY 201

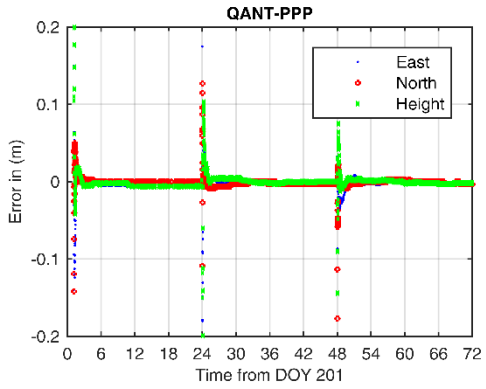
QANT-PPP
East
North
Height
Error in (m)
Time from DOY 201

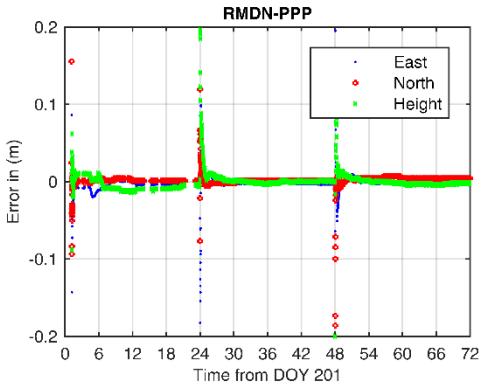
RMDN-PPP
East
North
Height
Error in (m)
Time from DOY 201

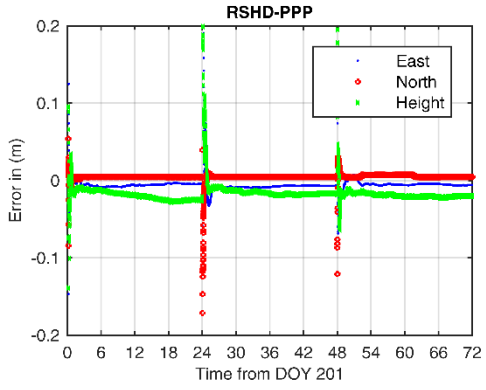
RSHD-PPP
East
North
Height
Error in (m)
Time from DOY 201

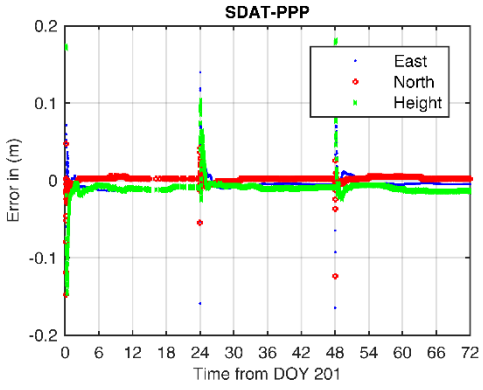
SDAT-PPP
East
North
Height
Error in (m)
Time from DOY 201

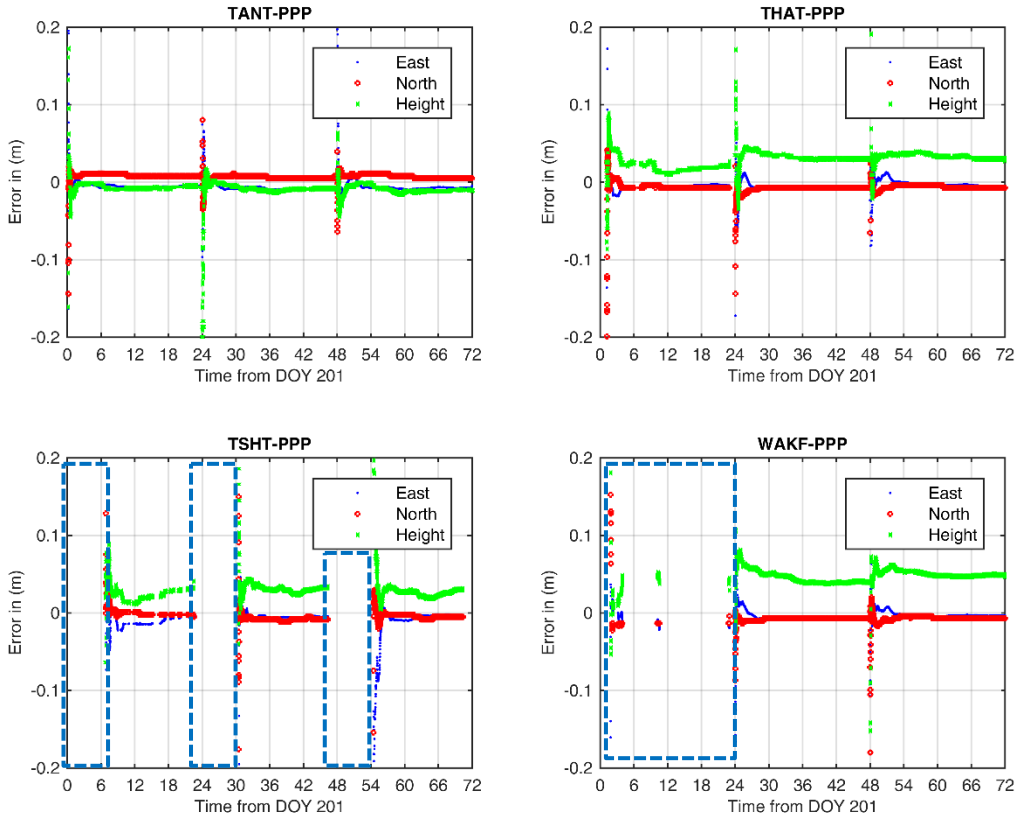

Figure 6. Dual PPP errors for ESA-CORS stations (epoch-wise mode)

b) **IGS-CORS:**

Figure 7 presents the PPP errors in the east, north, and height directions; in addition, Table 6 shows the detailed statistics of the PPP solution (max., min., average, RMS, SD, and $SD_{95\%}$). For DOY201, the horizontal error showed up to 3 mm (μ = 1.7 mm). Further analysis showed that the obtained RMSE was 1.7 mm (SD = 1.2 mm). For the height direction, the component presented an error of up to 8 mm (μ = 3.3 mm). As shown in Table 6, the obtained RMSE was 4.5 mm with an SD of 3.3 mm. Regarding DOY202, the component showed an error of up to 2 mm for horizontal (μ = 1.0–1.2 mm) and up to 13 mm (μ = 5.5 mm) for height directions. It is clear from this table that the RMSE had values of 1.3–1.5 mm (SD was circa 1 mm) and 6.7 mm (SD was circa 4 mm).

Finally, from Table 6, the error obtained in DOY203 for the east direction was up to 4 mm (μ = 1.2 mm) with an RMSE of 1.8 mm (SD = 1.5 mm). For north direction, the obtained error was up to 2 mm (μ = 1.2 mm) with an RMSE of 1.2 mm (SD = 1.2 mm). According to these data, we can infer that the error in height was between 2 and 5 mm (μ = 3 mm) with an RMSE of 3.2 mm (SD = 1.3 mm). In summary, these results show that the horizontal error was up to 3 mm (μ = 1.2 mm) with an RMSE value of about 1.5 mm (SD was circa 1.2 mm). Further, the height error was up to 8 mm with an RMSE of 5 mm (SD was about 3 mm). This study shows that $SD_{95\%}$ was less than 1 mm for horizontal and 1.2 mm for height directions after eliminating the outliers. Finally, Figure 8 presents the epoch-wise analysis for the stations; it is clear that IGS stations had continuous observation data.

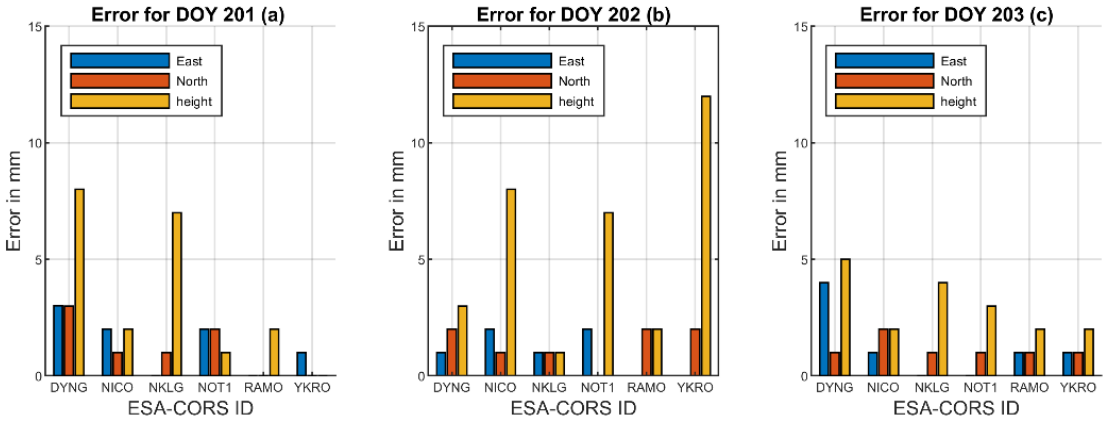

Figure 7. Dual PPP errors for IGS-CORS: (a) for DOY 201, (b) for DOY 202, and (c) for DOY 203 (static mode)

Table 6. Statistics of static-PPP solution for IGS-CORS in millimeters

	DOY201			**DOY202**			**DOY203**			**Mean**		
	E	**N**	**h**	**E**	**N**	**h**	**E**	**N**	**h**	**E**	**N**	**h**
Max.	3.0	3.0	8.0	2.0	2.0	12.0	4.0	2.0	*5.0*	3.0	2.3	8.3
μ	1.3	1.2	3.3	1.0	1.3	5.5	1.2	1.2	3.0	1.2	1.2	3.9
Min.	0.0	0.0	0.0	0.0	0.0	1.0	0.0	1.0	2.0	0.0	0.3	1.0
RMSE	1.7	1.6	4.5	1.3	1.5	6.7	1.8	1.2	3.2	1.6	1.4	4.8
SD	1.2	1.2	3.3	0.9	0.8	4.2	1.5	1.2	1.3	1.2	1.1	2.9
$SD_{95\%}$	1.0	0.8	1.0	0.9	0.8	1.0	0.5	0.8	1.3	0.8	0.8	1.1

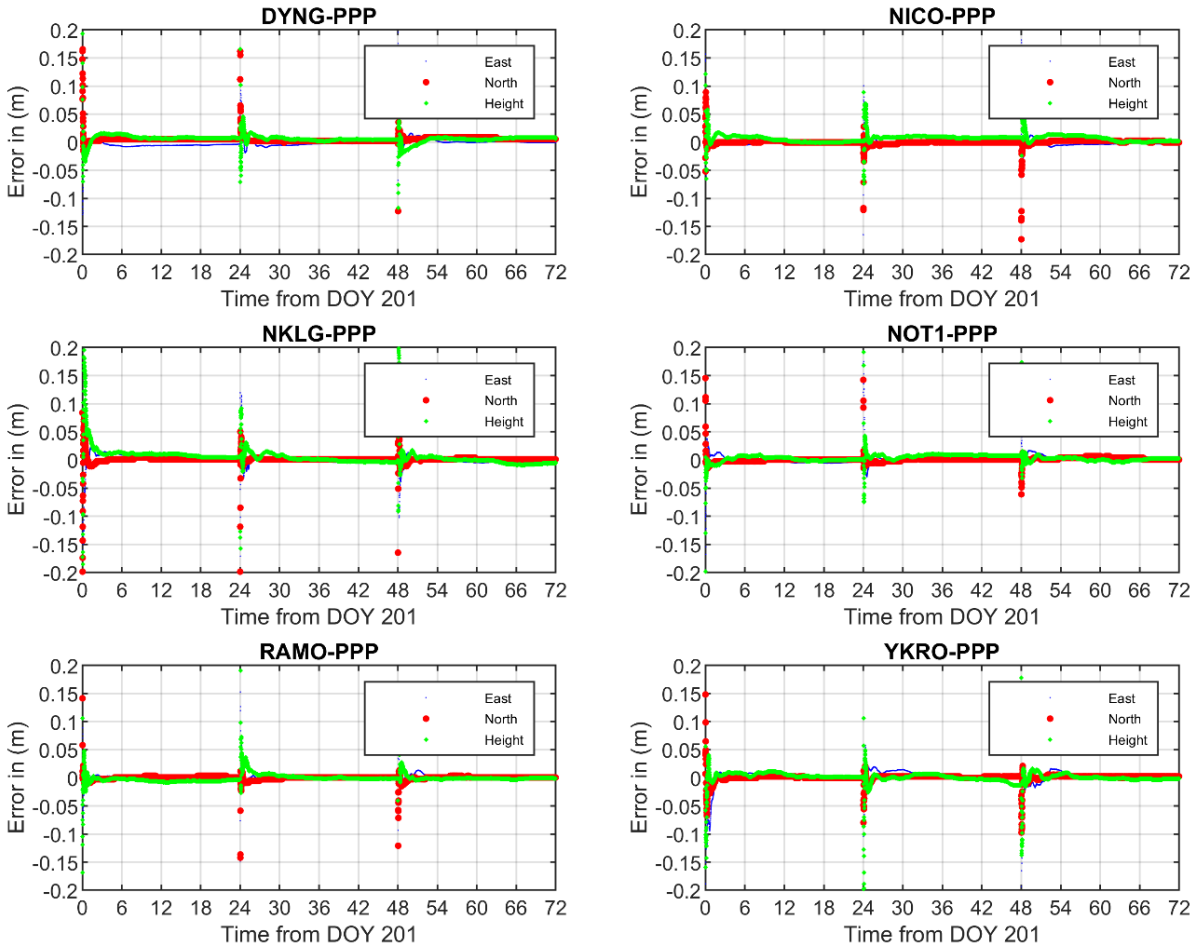

Figure 8. Dual PPP errors for IGS-CORS stations (epoch-wise mode)

5. CONCLUSIONS

Establishing GNSS CORS in Egypt is considered one of the main means to provide precise positioning and navigation for all development applications. This study provided a framework for investigating the accuracy of 32 ESA-CORS in addition to six IGS-CORS. Three consecutive observation days were analyzed using CSRS-PPP's free PPP online service.

The overall PPP solution for ESA-CORS showed up to 13 mm errors with a mean value μ of 4–6 mm in the horizontal direction. The results indicated that the RMSE value was 6 mm (SD = 3–4 mm). The solution had up to 47 mm (μ was circa 18 mm) error for height direction with an RMSE value of 22 mm (SD was circa 14 mm). By excluding the outliers, the current study found that $SD_{95\%}$ was 2 mm for east and north directions and 6–7 mm for height direction. The extreme height errors seen in stations BLTM, ISAN, LXOR, MNSH, MOUS, QANA, THAT, TSHT, and WAKF are explained by the loss of the observation data due to data transmission via GSM from the receiver onsite to the center of Cairo. These results matched similar regional results obtained by Abdallah (2015), Abdallah and Schwieger (2016), and Jamieson and Gillins (2018) in east, north, and height directions.

Regarding the PPP solution for six IGS-CORS, this study has shown that the errors for East and North were up to 3 mm with a mean value of 1.2 mm (RMSE was circa 1.5 mm). In the height direction, the PPP solution was up to 8 mm (μ was circa 4 mm) with an RMSE of 5 mm. This study shows that the SD95% value was less than 1 mm for horizontal and 1.2 mm for height direction. This accuracy delivered by IGS-CORS is two times better for horizontal and four times better for height direction than the one obtained from ESA-CORS.

Acknowledgment. The authors are very grateful to the Egyptian Surveying Authority (ESA) for providing Rinex observation data for the processed Egyptian Surveying Authority (ESA)-continuously operating reference stations (CORS).

REFERENCE

Abdallah A. (2015) The Effect of Convergence Time on the Static- PPP Solution. Proceedings of the 2nd International workshop on "Integration of Point- and Area-wise Geodetic Monitoring for Structures and Natural Objects. Institute of Engineering Geodesy, March, 27-29, Stuttgart, Germany.

Abdallah A. and Schwieger V. (2016) Static GNSS Precise Point Positioning using free online services for Africa. *Survey Review*, V. 48, No. 346, 61-77.

Ayhan, ME and Almuslmani, B. (2021) Positional accuracy and convergence time assessment of GPS precise point positioning in static mode, *Arabian Journal of Geosciences*, V. 14, No. 13, 1-12.

Bar-Sever, Y. E., Kroger, P. M., and Borjesson, J. A. (1998) Estimating horizontal gradients of tropospheric path delay with a single GPS receiver. *Journal of Geophysical Research: Solid Earth*, V. 103, No. (B3), 5019-5035.

Boehm, J., Werl, B., and Schuh, H. (2006) Troposphere mapping functions for GPS and very long baseline interferometry from European Centre for Medium-Range Weather Forecasts operational analysis data. *Journal of geophysical research: solid earth*, V. 111, No. B2.

Böhm, J and Schuh, H. (2004) Vienna mapping functions in VLBI analyses. *Geophysical research letters*, V. 31, No. 1.

CSRS-PPP 2021, The Canadian Spatial Reference System (CSRS) Precise Point Positioning (PPP), viewed 14 February 2021, <https://webapp.geod.nrcan.gc.ca/geod/tools-outils/ppp.php >.

Dach, R., Lutz S., Walser P., and Fridez P. (2015) Manual of Bernese GNSS Software Version 5.2, *University of Bern*, Switzerland.

El Manaily E., Abd Rabbou M., El-Shazly A., and Barakam M. (2017) Evaluation of quad-constellation GNSS precise point positioning in Egypt, *Artificial Satellites*, V. 52, No. 1, 9-18

El Shouny A., & Miky Y. (2019) Accuracy assessment of relative and precise point positioning online GPS processing services, *Applied Geodesy*. V. 13, No. 3, 215–227.

ESA (Egyptian Survey Authority) (2012) The processing report of the Egyptian virtual reference stations, Internal technical report, 276 pp.

Hofmann-Wellenhof B., Lichtenegger H., and Wasle E. (2008) GNSS: Global Navigation Satellite Systems. 1st edn. *Springer-Verlag Wien*.

Hopfield, H. (1969) Two-quartic tropospheric refractivity profile for correcting satellite data. *Journal of Geophysical research*, V. 74, No. 18, 4487-4499.

Isioye, O. A., Moses, M., and Abdulmumin, L. (2019) Comparative study of some online GNSS post-processing services at selected permanent GNSS sites in Nigeria. *Accuracy of GNSS methods*, pp. 89-106.

ITRF (2020) *International Terrestrial Reference Frame*, <http://itrf.ensg.ign.fr/>.

Jamieson, M., & Gillins, D. T. (2018) Comparative analysis of online static GNSS postprocessing services. *Journal of Surveying Engineering*, V. 144, No. 4, 5018002.

Kedar, S., Hajj, G. A., Wilson, B. D., and Heflin, M. B. (2003) The effect of the second order GPS ionospheric correction on receiver positions. *Geophysical research letters*, V. 30, No. 16.

Kouba, J. (2009) Testing of global pressure/temperature (GPT) model and global mapping function (GMF) in GPS analyses. *Journal of Geodesy*, V. 83, No. 3, 199-208.

Le Provost, C., & Lyard, F. (1997) Energetics of the M2 barotropic ocean tides: an estimate of bottom friction dissipation from a hydrodynamic model. *Progress in Oceanography*, V. 40, No. 1-4, 37-52.

Mikhail, E. (1976) Observations and Least Squares. *New York: University Press of America*.

Mirsa, P., & Enge, P. (2012) Global Positioing System Signals, Measurements, and Performance. Revised second ed. *Lincoln: Ganga. Jamuna Press*.

NGS (2021), *(National Geodetic Survey)*, viewed 04 October 2021, <https://www.ngs.noaa.gov/ANTCAL/>.

Rabah M., Elmewafy M., and Farhan M. (2016) Datum maintenance of the main Egyptian geodetic control networks by utilizing Precise Point Positioning ‘‘PPP’’ technique, *NRIAG Journal of Astronomy and Geophysics*, V. 5, No. 1, 96-105.

Sakurai, T. (1985) Magnetic stellar winds-A 2-D generalization of the Weber-Davis model. *Astronomy and Astrophysics*, V. 152, 121-129.

Sanz J., Rovira-Garcia A., Hernández-Pajares M., Juan M., Ventura-Traveset J., López-Echazarreta C., and Hein G. (2012) The ESA/UPC GNSS-Lab Tool (gLAB): an advanced educational and professional package for GNSS data processing and analysis, in *6th ESA Workshop on Satellite Navigation Technologies Multi-GNSS Navigation Technologies. Noordwijk*, the Netherlands.

Snay, R. A., & Soler, T. (2008) Continuously operating reference station (CORS): history, applications, and future enhancements, *Journal of Surveying Engineering*, V. 134, No. 4, 95-104.

Walpersdorf, A., Bouin, M. N., Bock, O., and Doerflinger, E. (2007) Assessment of GPS data for meteorological applications over Africa: Study of error sources and analysis of positioning accuracy. *Journal of atmospheric and solar-terrestrial physics*, V. 69, N. 12, 1312-1330.

Zhou F., Dong D., Li W., Jiang X., Wickert J., and Schuh H. (2018) GAMP: An open-source software of multi-GNSS precise point positioning using undifferenced and uncombined observations, *GPS Solutions*, V. 22, No. 2, 33.

Zumberge J. F., Heftin M. B., Jefferson D., Watkins M. M., and Webb F. H. (1997) Precise point positioning for the efficient and robust analysis of GPS data from large networks, *Journal of Geophysical Research*, V. 102, No. 10, 5005-5017.

Received: *2020-10-21*

Reviewed: *2021-01-02 (J. Kalita); 2021-02-10 (G. Krzan); 2022-02-02 (undisclosed name)*

Accepted: *2022-03-04*